Thermal decomposition of barium ferrate(VI): Mechanism and formation of Fe^{IV} intermediate and nanocrystalline Fe$_2$O$_3$ and ferrite☆

Libor Machala [a, *], Virender K. Sharma [b], Ernö Kuzmann [c], Zoltán Homonnay [c], Jan Filip [a], Radina P. Kralchevska [a]

[a] Regional Centre of Advanced Technologies and Materials, Department of Experimental Physics, Faculty of Science, Palacký University, Olomouc, Czech Republic
[b] Department of Environmental and Occupational Health, School of Public Health, Texas A&M University, 1266 TAMU, College Station, TX 77843, USA
[c] Institute of Chemistry, Eötvös Loránd University, Budapest, Hungary

ABSTRACT

Simple high-valent iron-oxo species, ferrate(VI) (Fe^{VI}O$_4^{2-}$, Fe(VI)) has applications in energy storage, organic synthesis, and water purification. Of the various salts of Fe(VI), barium ferrate(VI) (BaFeO$_4$) has also a great potential as a battery material. This paper presents the thermal decomposition of BaFeO$_4$ in static air and nitrogen atmosphere, monitored by combination of thermal analysis, Mössbauer spectroscopy, X-ray powder diffraction, and electron-microscopic techniques. The formation of Fe^{IV} species in the form of BaFeO$_3$ was found to be the primary decomposition product of BaFeO$_4$ at temperature around 190 °C under both studied atmospheres. BaFeO$_3$ was unstable in air reacting with CO$_2$ to form barium carbonate and speromagnetic amorphous iron(III) oxide nanoparticles (<5 nm). Above 600 °C, a solid state reaction between BaCO$_3$ and Fe$_2$O$_3$ occurred, leading to the formation of barium ferrite nanoparticles, BaFe$_2$O$_4$ (20–100 nm).

© 2016 Elsevier B.V. All rights reserved.

1. Introduction

Oxidized iron usually exists in ferrous (Fe(II)) and ferric (Fe(III)) forms, but high-valent iron compounds of Fe(IV), Fe(V), and Fe(VI) have also been intensively studied in the last decade [1–4]. For example, several oxoiron(IV) (Fe^{IV}=O) and oxoiron(V) (Fe^{V}=O) complexes containing model organic ligands have been synthesized to understand the biological imperative of oxidative transformation in biological environment [5–11]. Another class of high-valent iron species are simple tetraoxy high-valent iron anions such as Fe^{IV}O$_4^{2-}$ (Fe(IV)), Fe^{V}O$_4^{3-}$ (Fe(V)), and Fe^{VI}O$_4^{2-}$ (Fe(VI)), commonly called ferrates. These have also been of great interest due to their potential in homogeneous water oxidation catalyst, energy storage, green chemistry oxidations, and detoxification of contaminants and toxins [12,13]. Examples of the application of Fe(VI) include generation of oxygen from water, production of super-iron batteries, selective conversion of alcohol to aldehyde, and oxidative transformation of cyanotoxins and antibiotics [12,14–19].

In the past few years, we have been interested in mechanistic studies on the reduction of Fe(VI) to answer whether the reactions go through either $1-e^-$ or $2-e^-$ transfer steps with the formation of Fe(V) and Fe(IV) intermediates, respectively, where Fe(III) and Fe(II) are final iron reduced species [13,19,20]. Some progress has been made by understanding relationships between reaction rates and thermodynamic potentials [21]. A handful studies on experimental evidences suggest both kinds of electron transfer mechanistic pathways [14,20,22]. The recent advancement in oxidative mechanism was possible due to improvement in analytical techniques.

A previous study on the thermal decomposition of potassium ferrate(VI) (K$_2$FeO$_4$) did not observe any intermediate iron species (i.e. Fe(V) and Fe(IV)), which are highly unstable [23]. However, recent work with synchrotron radiation using a nuclear forward scattering experimental technique clearly showed these unstable intermediate iron species [24]. The present paper focuses on barium ferrate(VI), BaFeO$_4$, which exhibited a high discharge performance at high current when applied as a battery material [25]. This performance may be related to the formation of a relatively stable intermediate with perovskite-like structure during decomposition of BaFeO$_4$. In contrast, the discharge intermediate of

---

☆ ESI available: additional Mössbauer and XRD spectra.
* Corresponding author.
  E-mail address: libor.machala@upol.cz (L. Machala).

K_2FeO_4 was very unstable and immediately converted to Fe(III) oxides [26,27]. Significantly, comprehending the decomposition mechanism of salts of Fe(VI) is of utmost importance to advancing the fundamental chemistry of ferrates, which may lead to simple synthesis of these compounds and an efficient performance of a super iron discharged battery. The aim of the current paper is the mechanistic understanding of the thermal decomposition of $BaFeO_4$.

A few reports on the decomposition of $BaFeO_4$ under thermal and humid conditions have conflicting findings in terms of intermediate iron oxidation state(s) and final iron oxide phases [26–32]. Our results in the current paper unequivocally demonstrate the formation of Fe(IV) as intermediate species and final nanoscale-iron oxide and -ferrite phases. The objectives of the article are to: (i) provide evidence of the electron transfer steps of decomposition of $BaFeO_4$ by using thermogravimetry (TG), differential scanning calorimetry (DSC), and Mössbauer spectroscopy techniques, (ii) distinguish decomposition of $BaFeO_4$ under static air and inert atmosphere, and (iii) learn the nature of reduced iron(III) oxide phases by applying low temperature (5 K)/in-field (5 T) Mössbauer spectroscopy, variable temperature X-ray diffraction (VT-XRD), and imaging (scanning electron microscopy (SEM) and transmission electron microscopy (TEM)) techniques.

2. Experimental details

2.1. Sample preparation

Barium ferrate(VI) was prepared by using a method reported earlier [33]. Briefly, a basic solution of the barium chloride was allowed reacting with a solution of K_2FeO_4 at 0 °C. Solutions used in this procedure were purged with nitrogen in order to minimize the presence of atmospheric CO_2. A rapid filtration of the barium ferrate(VI) obtained was carried out in order to increase the purity of product.

2.2. Techniques

Thermal analysis was carried out simultaneously in the thermogravimetric (TG) and calorimetric (DSC) analysis device (STA 449 °C, Netzsch). The samples were dynamically heated from 25 °C to 1000 °C in the dynamic atmospheres of argon and air (both with the flow of 30 ml/min) with a heating rate of 10 °C/min. Evolved gasses were analyzed using a mass spectrometry device (QMS 403 C, Aëolos).

X-ray powder diffraction (XRD) experiments were performed with a PANalytical X'Pert PRO instrument (CoK_α radiation) equipped with an X'Celerator detector and programmable divergence and anti-scatter slits. Standard samples were placed on a zero-background Si slides, gently pressed in order to obtain sample thickness of about 0.5 mm and scanned in the 2θ range of 10–90° in steps of 0.017°. The in-situ variable-temperature XRD measurement was performed in an X-ray reaction chamber XRK 900 (Anton Paar GmbH) under constant nitrogen flow (20 ml/min) and temperature range from 100 °C to 600 °C. The heating slope was 40 °C/min and XRD patterns were collected in steps of every 20 °C (2θ range of 20–60°; 10 min each scan). Therefore, the resulting slope was approximately 2 °C/min. In the reaction chamber, the powder sample was placed into the sample holder made of glass ceramics (Macor).

The transmission ^{57}Fe Mössbauer spectra were measured using a Mössbauer spectrometer in a constant acceleration mode with a $^{57}Co(Rh)$ source. The isomer shift values were related to metallic alpha iron at room temperature (RT). The measurements were carried out at 25 and 300 K in a zero external magnetic field as well

as at 5 K in an external magnetic field of 5 T, applied parallel to the direction of the gamma ray propagation. Low temperature and in-field measurements were conducted using a cryomagnetic system of Oxford Instruments. TEM images were obtained on JEOL 2010 instrument with LaB_6 cathode at accelerating voltage of 160 kV. SEM images were obtained on the field-emission scanning electron microscope (SU6600, Hitachi) working at 6 kV.

3. Results and discussion

3.1. Characterization of synthesized $BaFeO_4$

Initially, the as-prepared $BaFeO_4$ sample, labeled as BF, was analyzed by Mössbauer spectroscopy. A Mössbauer spectrum recorded at room temperature (RT), shown in Fig. S1a of the 'ESI', had a doublet (84.1% of spectral area) with hyperfine interaction parameters $\delta_{Fe} = -0.90$ mm/s, $\Delta E_Q = 0.17$ mm/s; typical for a hexavalent iron atom [34]. The minor doublet (15.9% of spectral area) with hyperfine interaction parameters $\delta_{Fe} = 0.31$ mm/s, $\Delta E_Q = 0.61$ mm/s was ascribed to (super)paramagnetic iron(III) oxides or oxyhydroxides.

Next, the XRD pattern of a BF sample was examined (Fig. S1b of the 'ESI'), which showed diffraction lines corresponding to only two crystalline phases, orthorhombic $BaCO_3$ and orthorhombic $BaFeO_4$. The observed weight ratio between $BaFeO_4$ and $BaCO_3$ is 85:15. Since no additional phase was observed in the XRD pattern, the Fe(III) phase identified in the Mössbauer spectroscopy measurement is therefore X-ray amorphous. The presence of $BaCO_3$ and Fe(III) were considered as impurities present in the initial BF sample.
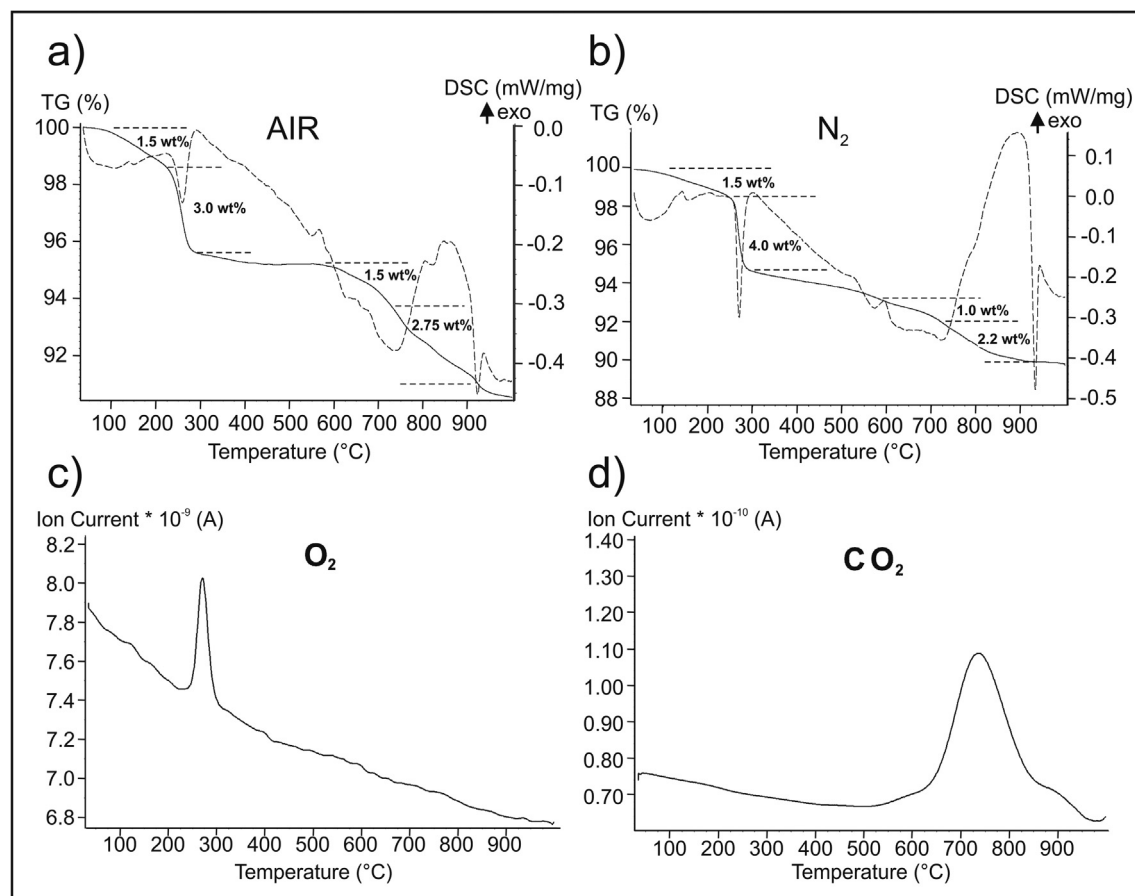
3.2. Thermal decomposition study

3.2.1. Thermal analysis

In this study, thermal decomposition of $BaFeO_4$ was first monitored in air by TG and DSC techniques. Fig. 1a shows three main decomposition steps. The first step was within a temperature range from 25 to 230 °C, which was ascribed to a dehydration of the sample. The second step started at 230 °C and was related to the decomposition of $BaFeO_4$. The second step was completed at 310 °C. It was accompanied by an endothermic effect, and mass loss was 3.0 wt%. The third step occurred within a broad temperature range from 600 °C to 920 °C; it exhibited two thermal effects on the DSC curve and overall mass loss was 4.25 wt%. The chemical transformation of barium carbonate describes the third step [35].

The results of thermal analysis of decomposition of the BF sample under an inert environment (i.e. Ar) are shown in Fig. 1b. Both the TG and DSC curves of the BF sample were very similar to those seen under air (Fig. 1b vs. Fig. 1a). The only significant difference was a slightly higher mass loss (4.0 wt%) observed in an inert atmosphere during the second decomposition step, which could be explained by the absence of carbon dioxide. As expected, the evolution of oxygen was detected within the second decomposition step (230–300 °C) by mass spectrometry of evolved gasses (Fig. 1c). The evolution of carbon dioxide, from $BaCO_3$, was observed in the temperature range from 550 to 1000 °C (Fig. 1d).

3.3. Mössbauer spectroscopy measurements

In the following parts, thermodynamic decomposition was examined by isothermal heating of the BF sample at different temperatures in air, followed by characterization of selected samples by Mössbauer spectroscopy. The BF sample was heated at 190 °C for 2 h, at 300 °C for 1 h, and at 600 °C for 1 h (each heat treatment started from the initial BF sample) and labeled as BF190,

Fig. 1. Thermal analysis and evolved gases analysis of the thermal decomposition of $BaFeO_4$. (a) Air, (b) N_2, (c) O_2 evolution, and (d) CO_2 evolution (TG-solid line, DSC- dashed line, heating rate 10 °C/min).

BF300A, and BF600, respectively. Part of the BF300A sample was further exposed to open air for six months (labeled as BF300B) and then it was characterized to learn the long-term stability of decomposed product in air.

The room temperature Mössbauer spectra of different samples are shown in Fig. 2 and the evaluated hyperfine interaction parameters are given in Table 1. The Mössbauer spectrum of the BF190 sample was characterized by three spectral components (Fig. 2a), which include a doublet corresponding to non-decomposed barium ferrate(VI), a singlet with an isomer shift of −0.28 mm/s, and a doublet with hyperfine interaction parameters typical for octahedrally coordinated Fe(III). A Mössbauer spectrum of BF300A sample, shown in Fig. 2b, indicates that the decomposition of $BaFeO_4$ is complete because the respective Fe(VI) doublet with isomer shift (≈ -0.9 mm/s) was not present in the spectrum.

The isomer shift of the singlet (≈ -0.27 mm/s), observed in the spectra of both BF190 and BF300A samples, was assigned to tetravalent iron atoms, based on known parameters reported in literature [36]. This assignment was further confirmed by performing Mössbauer measurement of the BF300A sample at low temperature ($T = 25$ K) (Fig. 3a). The spectrum contained a magnetically split Fe(IV) component with isomer shift of −0.19 mm/s (a second order Doppler shift has to be taken into account) and the relative area was almost the same as at room temperature (Table 1). Another two subspectra, doublet and sextet, corresponded to octahedrally coordinated Fe^{3+} atoms within a (super)paramagnetic and magnetically ordered fractions, respectively.

In the BF300B sample, Fe(IV) singlet was not observed (Fig. 2c). There is only one Fe(III) doublet, with quadrupole splitting slightly increased in comparison with the evaluated quadrupole splitting of BF300A sample. Mössbauer spectrum of BF600 sample at room temperature shows a dominant sextet (RA $\approx 60\%$) (Fig. 2d). The hyperfine interaction parameters of this sextet, reported in Table 1, are similar to those reported for barium ferrite(III) ($BaFe_2O_4$) with tetrahedrally coordinated trivalent iron in a spinel structure [37]. Singlet and doublet, which are present in the spectrum along with the barium ferrite sextet, belong to remaining Fe(IV) and Fe(III) phases identified in the samples heated at lower temperatures (compare hyperfine interaction parameters in Table 1).

3.4. X-ray diffraction study

The same samples as characterized in the previous sections were subjected to X-ray diffraction measurements (Fig. 4). The XRD pattern of the sample BF300A in Fig. 4a reveals the presence of orthorhombic (space group Pmcn) $BaCO_3$ and rhombohedral (space group R-3m) $BaFeO_3$ phases. On the other hand, BF300B sample had only diffraction lines of barium carbonate in its XRD pattern (Fig. 4b). No other crystalline phases were identified in the patterns of BF300A and BF300B samples. Thus, the Fe(III) phases suggested by Mössbauer spectroscopy are X-ray amorphous, similar to the initial BF sample. Besides the barium carbonate and barium iron(IV) oxide phases, previously identified in BF300A sample, the XRD pattern of BF600 sample had diffraction lines corresponding to orthorhombic barium ferrite ($BaFe_2O_4$) (Fig. 4c).
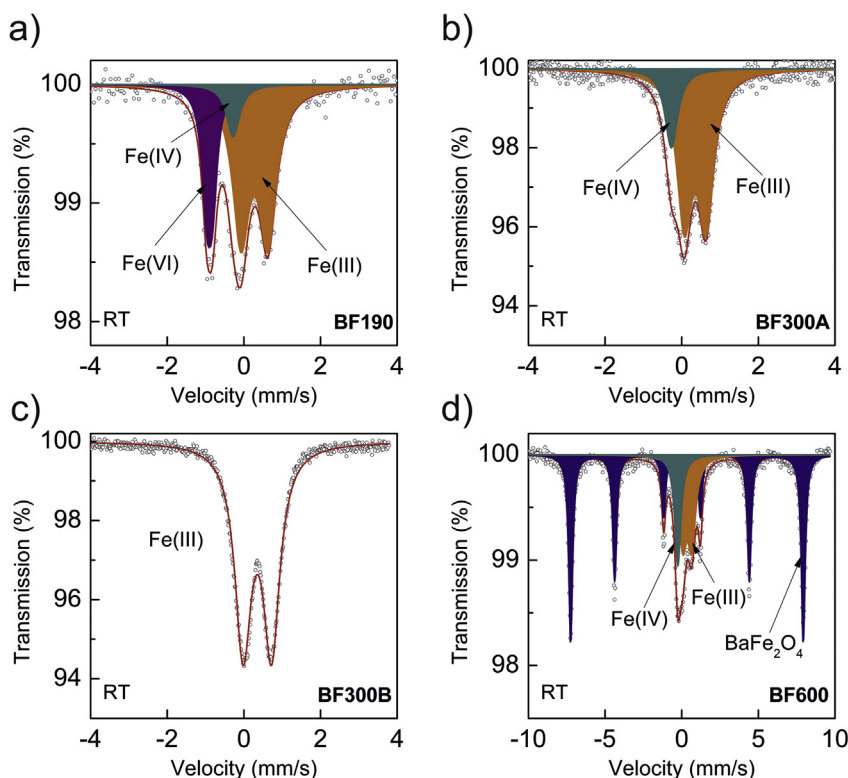
Fig. 2. Room temperature Mössbauer spectra for different samples. (a) BF190, (b) BF300A, (c) BF300B, and (d) BF600.

Table 1
Parameters of Mössbauer spectral components for samples BF190, BF300A, BF300B, and BF600.

Sample	T (K)	Component	δ_{Fe} (mm/s)	$\Delta E_Q(\varepsilon_Q)$ (mm/s)	B_{hf} (T)	LW (mm/s)	RA (%)
BF190	300	Fe(VI)	−0.90	0.15	−	0.31	25.2
		Fe(IV)	−0.28	0.00	−	0.42	8.9
		Fe(III)	0.28	0.70	−	0.54	65.9
BF300A	300	Fe(IV)	−0.27	0.00	−	0.41	18.7
		Fe(III)	0.35	0.56	−	0.49	81.3
	25	Fe(IV)	−0.19	0.04	23.2	1.01	19.0
		Fe(III)	0.45	0.55	−	1.35	41.4
		Fe(III)	0.46	−0.02	47.3	1.55	39.6
BF300B	300	Fe(III)	0.35	0.74	−	0.52	100
BF600	300	Fe(IV)	−0.25	0.00	−	0.50	14.1
		Fe(III)	0.36	0.59	−	0.63	25.9
		BaFe$_2$O$_4$	0.18	0.32	47.1	0.31	59.9

δ_{Fe}, isomer shift (related to metallic iron); ΔE_Q, quadrupole splitting; ε_Q, quadrupole shift; B_{hf}, hyperfine magnetic field; LW, full width at half maximum; RA, relative sub-spectrum area.

The thermal decomposition of BaFeO$_4$ under an inert environment was carried out by performing *in-situ* variable temperature XRD experiments in nitrogen atmosphere. Two representative XRD patterns measured at 300 °C and 600 °C are shown in Fig. 5. At 300 °C, two crystalline phases, rhombohedral BaFeO$_3$ and orthorhombic BaCO$_3$ (high temperature modifications) were identified. In comparison with the sample BF300A (see Fig. 4a), the relative BaFeO$_3$ content was significantly higher with respect to BaCO$_3$. This is consistent with the absence of gaseous CO$_2$ in the decomposition reaction. At 600 °C, in addition to BaFeO$_3$ diffraction peaks, orthorhombic BaFe$_2$O$_4$ was identified, the same as in the XRD pattern of the sample BF600 (see Fig. 4). However, the relative amount of BaFe$_2$O$_4$ was considerably lower in comparison with the sample BF600 due to lower content of BaCO$_3$.

3.5. Mechanism of BaFeO$_4$ thermal decomposition

The combination of thermal analysis, Mössbauer spectroscopy and X-ray powder diffraction unambiguously showed that the rhombohedral barium iron(IV) oxide, BaFeO$_3$, was the primary decomposition product of barium ferrate(VI) above 190 °C in air. The confidence in assigning the valence state of +4 lies in the low temperature Mössbauer measurements (see Fig. 3a, Table 1). The hyperfine field of ≈ 23 T, observed in the Mössbauer spectrum, is consistent with earlier reported value for BaFeO$_3$ [29,32]. This hyperfine field together with isomer shift of ≈ −0.15 mm/s (consider second order Doppler shift) is generally typical for tetravalent iron atoms in barium iron oxides [38,39]. To further confirm that no other iron bearing intermediates were formed during the decomposition of BaFeO$_4$ in air, *in-situ* high temperature (190 °C) Mössbauer spectrum was obtained. The results agreed with the *ex-situ* experiments, demonstrating only the Fe(IV) and Fe(III) phases again with a slightly higher content of BaFeO$_3$ (≈ 29% of spectral area).

Along with BaFeO$_3$, X-ray amorphous Fe(III) phase and barium carbonate were formed from initial barium ferrate(VI) thermally-
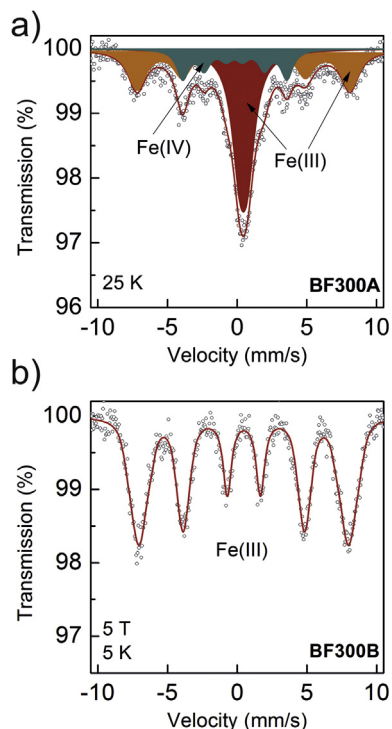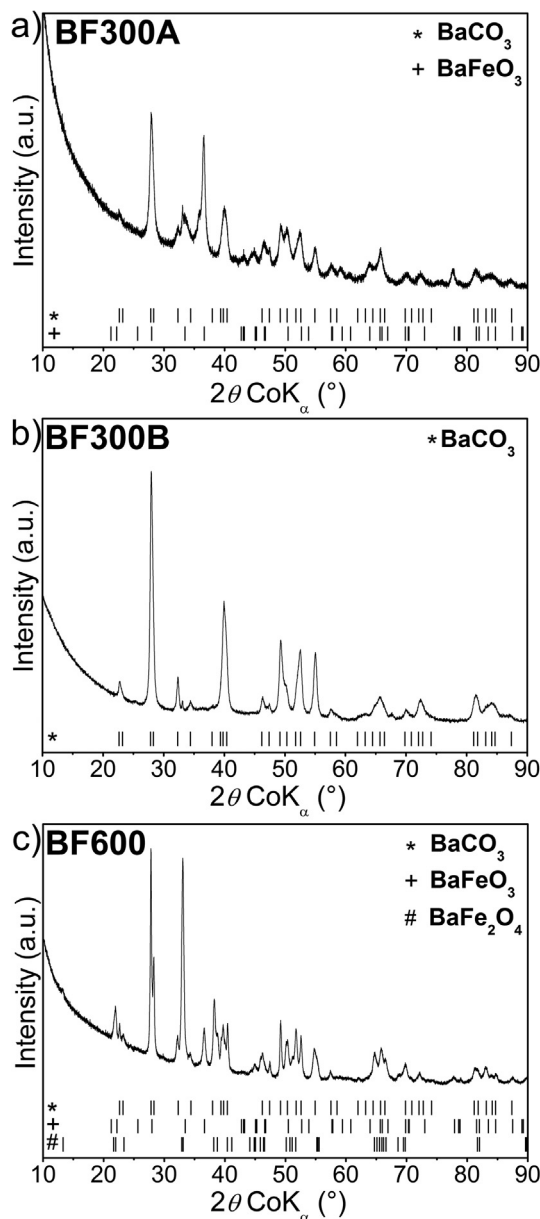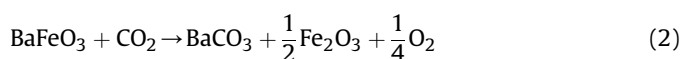
Fig. 3. a) Low temperature (25 K) Mössbauer spectrum of sample BF300A, b) low temperature (5 K)/in-field (5 T) Mössbauer spectrum of sample BF300B.

Fig. 4. XRD patterns of the samples BF300A (a), BF300B (b), BF600 (c). Peak labeling: * … BaCO$_3$ (PDF 00-005-0378), + … BaFeO$_3$ (PDF 01-074-0646), # … BaFe$_2$O$_4$ (PDF 00-025-1191).

treated in air. An Fe(III) phase was identified in all the examined samples (BF, BF190, BF300A, BF300B, BF600) as a super-paramagnetic doublet in the RT Mössbauer spectra with hyperfine interaction parameters typical for iron(III) oxides or oxyhydroxides. Apparently, the Fe(III) phase present in the initial BF sample showed practically the same RT Mössbauer spectral component as in the samples obtained by the thermal treatment. To determine chemical form, magnetic behavior, particle size, and morphology of the Fe(III) phase, the detailed analysis of the BF300B sample was carried out by low temperature (5 K)/in-field (5T) Mössbauer spectroscopy in combination with electron microscopy. In-field Mössbauer spectrum of BF300B sample, shown in Fig. 3b, was evaluated by one sextet component ($\delta_{Fe} = 0.46$ mm/s, $\varepsilon_Q = -0.02$ mm/s, $B_{eff} = 46.6$ T) with the ratios of intensities of spectral lines very close to 3:2:1:1:2:3, which were also observed in a zero-field Mössbauer spectrum (data not shown). Such character of Mössbauer spectra was assigned to speromagnetic behavior of the Fe(III) phase, showing that the application of an external magnetic field did not induce any long-range ordering in the structure due to the absence of the principal crystallographic axis in amorphous particles [40]. Since the formation of iron(III) oxy-hydroxides or hydrated forms of iron(III) oxides was not likely to occur at high temperature, the assumption was made that this phase was an amorphous anhydrous iron(III) oxide. TEM and SEM images, presented in Fig. 6, confirm the formation of BaCO$_3$ crystals which were partially covered by ultra-small Fe$_2$O$_3$ nanoparticles (<5 nm).

The mechanism of thermal decomposition of barium ferrate(VI) at 300 °C in static air may thus be described by the following reactions:

$$BaFeO_4 \rightarrow BaFeO_3 + \frac{1}{2}O_2 \tag{1}$$

$$BaFeO_3 + CO_2 \rightarrow BaCO_3 + \frac{1}{2}Fe_2O_3 + \frac{1}{4}O_2 \tag{2}$$

Reaction (2) shows the participation of CO$_2$ from the air in the reaction mechanism of thermal decomposition of BaFeO$_4$ at high temperature and also in the sample exposed to air after heating at 300 °C at room temperature (i.e. BF300B). The presence of carbon dioxide, therefore, caused the degradation of BaFeO$_3$. At 600 °C, the solid state reaction between the Fe$_2$O$_3$ formed in reaction (2) and BaCO$_3$ resulted in the formation of BaFe$_2$O$_4$ (reaction 3):

$$Fe_2O_3 + BaCO_3 \rightarrow BaFe_2O_4 + CO_2 \tag{3}$$
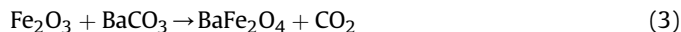
The solid state reaction between α-Fe$_2$O$_3$ and BaCO$_3$ leading to BaFe$_2$O$_4$ was also observed in the temperature range of 540–590 °C by other researchers [41]. The TEM image shows that barium ferrite
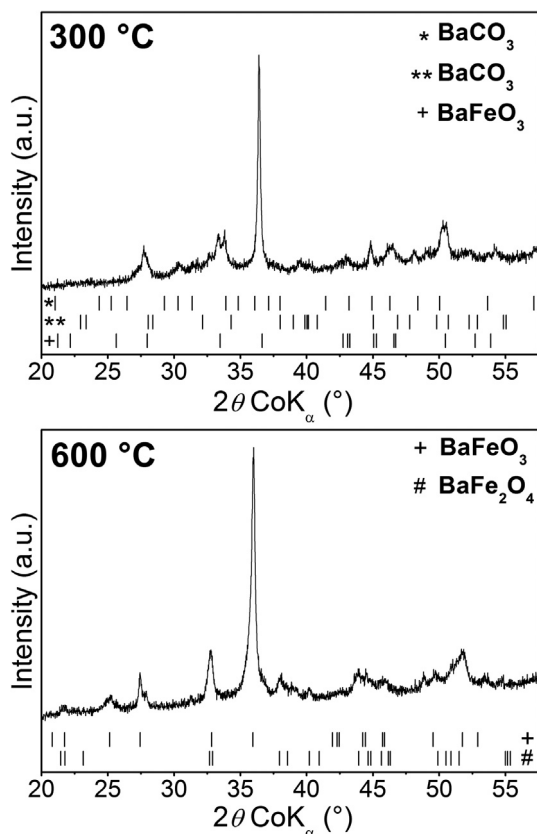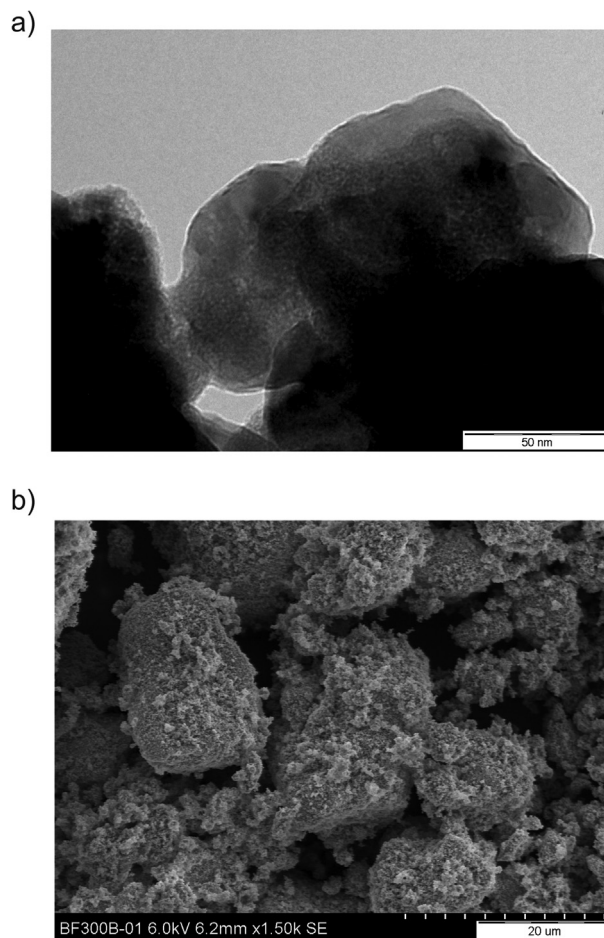
Fig. 5. XRD patterns recorded during *in-situ* variable temperature measurement at 300 °C (up) and 600 °C (down) in nitrogen atmosphere starting from the initial BF sample. Peak labeling: * ... BaCO$_3$ (PDF 00-052-1528), ** ... BaCO$_3$ (PDF 00-041-0373), + ... BaFeO$_3$ (PDF 01-074-0646), # ... BaFe$_2$O$_4$ (PDF 00-025-1191).

Fig. 6. TEM (a) and SEM (b) images of BF300B sample.

Fig. 7. TEM image of BF600 sample.

in sample BF600 formed nanoparticles with a broad particle size distribution (20–100 nm) (Fig. 7).
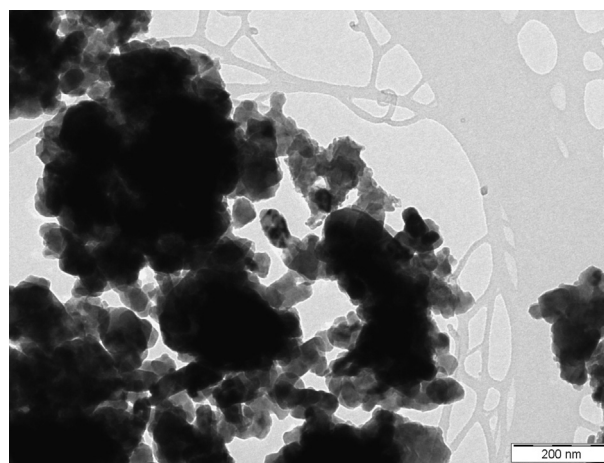
The suggested decomposition mechanism of BaFeO$_4$ agrees very well with thermal analysis of air samples (Fig. 1a). A theoretical value of mass loss related to the complete decomposition of BaFeO$_4$ to BaFeO$_3$ was estimated to be 5.16 wt%. This calculation considered the initial impurity of the BF sample as 15 wt% of Fe$_2$O$_3$ and consequently the corresponding amount of BaCO$_3$. The significantly lower value of mass loss observed (3.0 wt%) within the second decomposition step (between 230 and 310 °C) in air can be explained by a participation of gaseous CO$_2$ in the reaction, resulting in the formation of additional barium carbonate in the sample. A broad endothermic effect on DSC curve with the peak at 730 °C and corresponding mass loss of ≈ 1.5 wt% were related to the solid-state reaction of Fe$_2$O$_3$ with BaCO$_3$ (reaction 3). The decomposition of barium carbonate to barium oxide and carbon dioxide takes place as a competitive process above 730 °C (Fig. 1a), which was seen in a broad exothermal effect and mass loss of 2.75 wt% on DSC/TG curves.

4. Conclusions

The presented results clearly demonstrate that the first step of thermal decomposition of BaFeO$_4$ is the formation of Fe^{IV} species in the form of BaFeO$_3$ under both static air and inert environment. The subsequent reaction of BaFeO$_3$ with CO$_2$ in air at high temperature results in the formation of Fe(III) and barium carbonate. This re-action also occurred during the aging of BaFeO$_3$. The Fe(III) phase, which was formed by the transformation of BaFeO$_3$, was identified as amorphous Fe$_2$O$_3$ in the form of nanoparticles. Above 600 °C, carbon dioxide was evolved in the two competitive processes including the solid state reaction of barium carbonate with iron(III) oxide and the decomposition of barium carbonate. Future work may include *in-situ* high temperature Mössbauer and XRD mea-surements under rigorously inert atmosphere with pure BaFeO$_4$ sample without any presence of CO$_2$. This will further clarify the role of CO$_2$ in thermal decomposition of BaFeO$_4$. Similar studies can

be extended to other salts of Fe(VI) to learn the role of cations in finding the intermediate iron species. Furthermore, decomposition studies of salts of Fe(V) and Fe(IV) will advance the understanding of the chemistry of these high-valent iron compounds. Last but not least, understanding of reversibility of the proposed transformation reactions can be important in electrochemical applications of barium ferrate(VI).

Acknowledgements

Appendix A. Supplementary data

Supplementary data related to this article can be found at http://dx.doi.org/10.1016/j.jallcom.2016.01.185.

References

[1] L.L. Tang, W.A. Gunderson, A.C. Weitz, M.P. Hendrich, A.D. Ryabov, T.J. Collins, Activation of dioxygen by a TAML activator in reverse micelles: characterization of an Fe$^{(III)}$Fe$^{(IV)}$ dimer and associated catalytic chemistry, J. Am. Chem. Soc. 137 (30) (2015) 9704–9715, http://dx.doi.org/10.1021/jacs.5b05229.
[2] J.F. Berry, E. Bill, E. Bothe, S.D. George, B. Mienert, F. Neese, K. Wieghardt, An octahedral coordination complex of iron(VI), Science 312 (5782) (2006) 1937–1941, http://dx.doi.org/10.1126/science.1128506.
[3] W. Nam, Synthetic mononuclear nonheme iron−oxygen intermediates, Accounts Chem. Res. 48 (8) (2015) 2415–2423, http://dx.doi.org/10.1021/acs.accounts.5b00218 pMID: 26203519.
[4] S. Hong, H. So, H. Yoon, K.-B. Cho, Y.-M. Lee, S. Fukuzumi, W. Nam, Reactivity comparison of high-valent iron(IV)-oxo complexes bearing n-tetramethylated cyclam ligands with different ring size, Dalton Trans. 42 (2013) 7842–7845, http://dx.doi.org/10.1039/C3DT50750E.
[5] J. Hohenberger, K. Ray, K. Meyer, The biology and chemistry of high-valent iron-oxo and iron-nitrido complexes, Nat. Commun 3 (2012) 720, http://dx.doi.org/10.1038/ncomms1718.
[6] E.V. Kudrik, P. Afanasiev, L.X. Alvarez, P. Dubourdeaux, M. Clémancey, J.-M. Latour, G. Blondin, D. Bouchu, F. Albrieux, S.E. Nefedov, A.B. Sorokin, An n-bridged high-valent diiron-oxo species on a porphyrin platform that can oxidize methane, Nat. Chem. 4 (2012) 1024–1029, http://dx.doi.org/10.1038/nchem.1471.
[7] M. Puri, J. Lawrence Que, Toward the synthesis of more reactive s = 2 nonheme oxoiron(IV) complexes, Acc. Chem. Res. 48 (8) (2015) 2443–2452, http://dx.doi.org/10.1021/acs.accounts.5b00244 pMID: 26176555.
[8] M. Ansari, N. Vyas, A. Ansari, G. Rajaraman, Dalton Trans. 44 (2015) 15232–15243, http://dx.doi.org/10.1039/c5dt01060h.
[9] S. Fukuzumi, Electron transfer and catalysis with high-valent metal-oxo complexes, Dalton Trans. 44 (2015) 6696–6705, http://dx.doi.org/10.1039/C5DT00204D.
[10] J.T. Groves, Enzymatic C-H bond activation: using push to get pull, Nat. Chem. 6 (2014) 89–91, http://dx.doi.org/10.1038/nchem.1855.
[11] T. Chantarojsiri, Y. Sun, J.R. Long, C.J. Chang, Water-soluble iron(IV)-oxo complexes supported by pentapyridine ligands: axial ligand effects on hydrogen atom and oxygen atom transfer reactivity, Inorg. Chem. 54 (12) (2015) 5879–5887, http://dx.doi.org/10.1021/acs.inorgchem.5b00658 pMID: 26039655.
[12] R. Sarma, A.M. Angeles-Boza, D.W. Brinkley, J.P. Roth, Studies of the di-iron(VI) intermediate in ferrate-dependent oxygen evolution from water, J. Am. Chem. Soc. 134 (37) (2012) 15371–15386, http://dx.doi.org/10.1021/ja304786s pMID: 22900971.
[13] V.K. Sharma, R. Zboril, R.S. Varma, Ferrates: greener oxidants with multimodal action in water treatment technologies, Acc. Chem. Res. 48 (2) (2015) 182–191, http://dx.doi.org/10.1021/ar5004219 pMID: 25668700.
[14] Y. Lee, R. Kissner, U. von Gunten, Reaction of ferrate(VI) with ABTS and self-decay of ferrate(VI): kinetics and mechanisms, Environ. Sci. Technol. 48 (9) (2014) 5154–5162, 08073.
[15] M. Farmand, D. Jiang, B. Wang, S. Ghosh, D. Ramaker, S. Licht, Super-iron nanoparticles with facile cathodic charge transfer, Electrochem. Commun. 13 (9) (2011) 909–912 doi:http://dx.doi.org/10.1016/j.elecom.2011.03.039.
[16] L. Delaude, P. Laszlo, A novel oxidizing reagent based on potassium ferrate(VI) 1, J. Org. Chem. 61 (18) (1996) 6360–6370, http://dx.doi.org/10.1021/jo960633p pMID: 11667478.
[17] A. Karlesa, G.A.D.D. Vera, M.C. Dodd, J. Park, M.P.B. Espino, Y. Lee, Ferrate(VI) oxidation of β-lactam antibiotics: reaction kinetics, antibacterial activity changes, and transformation products, Environ. Sci. Technol. 48 (17) (2014) 10380–10389, http://dx.doi.org/10.1021/es5028426 pMID: 25073066.
[18] W. Jiang, L. Chen, S.R. Batchu, P.R. Gardinali, L. Jasa, B. Marsalek, R. Zboril, D.D. Dionysiou, K.E. O'Shea, V.K. Sharma, Oxidation of microcystin-lr by ferrate(VI): kinetics, degradation pathways, and toxicity assessments, Environ. Sci. Technol. 48 (20) (2014) 12164–12172.
[19] V.K. Sharma, Ferrate (VI) and ferrate (V) oxidation of organic compounds: kinetics and mechanism, Coord. Chem. Rev. 257 (2) (2013) 495–510.
[20] E.M. Casbeer, V.K. Sharma, Z. Zajickova, D.D. Dionysiou, Kinetics and mechanism of oxidation of tryptophan by ferrate (VI), Environ. Sci. Technol. 47 (9) (2013) 4572–4580.
[21] V.K. Sharma, Oxidation of inorganic compounds by ferrate (VI) and ferrate (V): one-electron and two-electron transfer steps, Environ. Sci. Technol. 44 (13) (2010) 5148–5152.
[22] V.K. Sharma, G.W. Luther, F.J. Millero, Mechanisms of oxidation of organo-sulfur compounds by ferrate (VI), Chemosphere 82 (8) (2011) 1083–1089.
[23] L. Machala, R. Zboril, V.K. Sharma, J. Filip, O. Schneeweiss, Z. Homonnay, Mössbauer characterization and in situ monitoring of thermal decomposition of potassium ferrate (VI), K$_2$FeO$_4$ in static air conditions, J. Phys. Chem. B 111 (16) (2007) 4280–4286.
[24] L. Machala, V. Procházka, M. Miglierini, V.K. Sharma, Z. Marušák, H.-C. Wille, R. Zbořil, Direct evidence of Fe(V) and Fe(IV) intermediates during reduction of Fe(VI) to Fe(III): a nuclear forward scattering of synchrotron radiation approach, PCCP 17 (34) (2015) 21787–21790.
[25] S. Licht, R. Tel-Vered, L. Halperin, Toward efficient electrochemical synthesis of Fe(VI) ferrate and super-iron battery compounds, J. Electrochem. Soc. 151 (1) (2004) A31–A39.
[26] K.E. Ayers, N.C. White, Characterization of iron(VI) compounds and their discharge products in strongly alkaline electrolyte, J. Electrochem. Soc. 152 (2) (2005) A467–A473.
[27] W. Yang, J. Wang, T. Pan, F. Cao, J. Zhang, C.-n. Cao, Physical characteristics, electrochemical behavior, and stability of BaFeO$_4$, Electrochim. Acta 49 (21) (2004) 3455–3461.
[28] R. Scholder, Alkali oxometallates(V) of chromium, manganese, iron, and cobalt, Bull. Soc. Chim. Fr. 4 (1965) 1112–1114.
[29] T. Ichida, Mössbauer study of the thermal decomposition products of BaFeO$_4$, J. Solid State Chem. 7 (3) (1973) 308–315.
[30] X.-M. Ni, M.-R. Ji, Z.-P. Yang, H.-G. Zheng, Preparation and structure characterization of nanocrystalline BaFeO$_4$, J. Cryst. Growth 261 (1) (2004) 82–86.
[31] J. Madarász, R. Zbořil, Z. Homonnay, V.K. Sharma, G. Pokol, Thermal decomposition of iron (VI) oxides, K$_2$FeO$_4$ and BaFeO$_4$, in an inert atmosphere, J. Solid State Chem. 179 (5) (2006) 1426–1433.
[32] I. Nowik, R. Herber, M. Koltypin, D. Aurbach, S. Licht, Mössbauer spectroscopic studies of the disintegration of hexavalent iron compounds (BaFeO$_4$ and K$_2$FeO$_4$), J. Phys. Chem. Solids 66 (7) (2005) 1307–1313.
[33] J. Gump, W. Wagner, J. Schreyer, Preparation and analysis of barium ferrate(VI), Anal. Chem. 26 (12) (1954), 1957–1957.
[34] V.K. Sharma, S.K. Dedushenko, Croat. Chem. Acta (2016). In press.
[35] I. Arvanitidis, D. Siche, S. Seetharaman, A study of the thermal decomposition of BaCO$_3$, Metall. Mater. Trans. B 27 (3) (1996) 409–416.
[36] I. Kokarovtseva, I. Belyaev, L. Semenyakova, Oxygen compounds of iron (VI, V, IV), Russ. Chem. Rev. 41 (11) (1972) 929–937.
[37] Y. Yang, Y. Jiang, Y. Wang, Y. Sun, L. Liu, J. Zhang, Influences of sintering atmosphere on the formation and photocatalytic property of BaFe$_2$O$_4$, Mater. Chem. Phys. 105 (2) (2007) 154–156.
[38] S. Morimoto, K. Kuzushita, S. Nasu, Mössbauer study of charge disproportionate BaFeO$_{3-y}$ and Ba$_{0.9}$Sr$_{0.1}$O$_{3-y}$ with 6H-perovskite structure, J. Magn. Magn. Mater. 272 (2004) 127–129.
[39] H. Kobayashi, F. Iga, Y. Nishihara, Study on the hexagonal BaFeO$_{3-y}$ system by the Mössbauer effect, Nucl. Instrum. Methods Phys. Res. Sect. B 76 (1) (1993) 258–259.
[40] L. Machala, R. Zboril, A. Gedanken, Amorphous iron(III) oxide a review, J. Phys. Chem. B 111 (16) (2007) 4003–4018.
[41] B. Randhawa, M. Kaur, Application of Mössbauer spectroscopy to the thermal decomposition of strontium and barium bis (CITRATO) ferrates(III), Hyperfine Interact. 188 (1−3) (2009) 95–101.